



Cite this: *Mol. Syst. Des. Eng.*, 2025, 10, 264

# A bio-inspired approach to engineering water-responsive, mechanically-adaptive materials†

Daseul Jang, <sup>a</sup> Yu-Tai Wong <sup>b</sup> and LaShanda T. J. Korley <sup>\*ab</sup>

Inspired by a diverse array of hierarchical structures and mechanical function in spider silk, we leverage building blocks that can form non-covalent interactions to develop mechanically-tunable and water-responsive composite materials *via* hydrogen bonding modulation. Specifically, self-assembling peptide blocks consisting of poly( $\beta$ -benzyl-L-aspartate) (PBLA) are introduced into a hydrophilic polyurea system. Using these peptide-polyurea hybrids (PPUs) as a hierarchical matrix, cellulose nanocrystals (CNCs) are incorporated to diversify the self-assembled nanostructures of PPUs through matrix-filler interactions. Our findings reveal that higher PBLA content in the PPUs reduces the magnitude of the stiffness differential due to the physical crosslinking induced by the peptide blocks. Additionally, the inclusion of CNCs in the PPU matrix increases the storage modulus in the dry state ( $E'_{\text{dry}}$ ) but also diminishes the wet-state modulus ( $E'_{\text{wet}}$ ) due to the shift of physical associations from peptidic arrangements to PBLA-CNC interactions, resulting in variations in the morphology of the PPU/CNC nanocomposites. This molecular design strategy allows for the development of adaptable materials with a broad range of water-responsive storage modulus switching ( $E'_{\text{dry}} - E'_{\text{wet}}$ ), spanning from  $\sim 70$  MPa to  $\sim 400$  MPa. This investigation highlights the potential of harnessing peptide assembly and peptide-cellulose interactions to achieve mechanical enhancement and water-responsiveness, providing insights for engineering next-generation responsive materials.

Received 1st November 2024,  
Accepted 5th February 2025

DOI: 10.1039/d4me00177j

rsc.li/molecular-engineering

## Design, System, Application

We present a bio-inspired strategy for engineering water-triggered, mechanically adaptive materials that draws inspiration from the tunable properties of spider silk. Our design focuses on developing a new class of water-responsive nanocomposites that utilize a peptide-containing polymer matrix combined with nanocellulose. By leveraging non-covalent interactions and dynamic hydrogen bonding similar to spider silk, we can achieve a diverse range of architectures and mechanical responses. This molecular design approach enables the nanocomposites to exhibit reversible changes in storage modulus when exposed to water, with values spanning from approximately 70 MPa to 400 MPa depending on the extent of peptide-cellulose interactions and hierarchical arrangements. The potential applications of these materials are vast, including biomedical devices, smart textiles, and aerospace structures, where adaptability and responsiveness to moisture are crucial. Our work will offer a deeper understanding of how molecular-level design can inform systems-level functionality, driving forward the development of next-generation smart materials.

## 1. Introduction

Stimuli-responsive materials are an exciting area of research due to their ability to change their shape and properties upon application of external triggers, including heat, light, water, electricity, and magnetic fields.<sup>1–3</sup> Water is an ideal trigger, particularly for biological applications, because it is a safe and ubiquitous stimulus for living organisms.<sup>4</sup> Water-

responsive materials can change their mechanical properties (*e.g.*, storage modulus) upon exposure to an aqueous environment, holding great potential for diverse application fields, including biomedical devices, smart textiles, aerospace structures, and adhesives.<sup>5–7</sup> These mechanically-adaptive polymeric materials are often developed *via* a composite approach by introducing hydrophilic nanocellulose (*i.e.*, filler) into a continuous polymer matrix, such as poly(ethylene oxide-*co*-epichlorohydrin) (EO-EPI),<sup>8</sup> poly(vinyl acetate),<sup>9</sup> polybutadiene,<sup>10</sup> natural rubber,<sup>7</sup> and polyurethane.<sup>11</sup> In these systems, their water-triggered modulus switching is driven by disruption of reversible hydrogen bonds. Thus, the extent of hydrogen bonding plays a crucial role in the mechanical response to water. Despite the development of various mechanically-adaptive materials,

<sup>a</sup> Department of Materials Science and Engineering, University of Delaware, 127 The Green, 201 Dupont Hall, Newark, Delaware, 19716, USA.

E-mail: lkorley@udel.edu

<sup>b</sup> Department of Chemical and Biomolecular Engineering, University of Delaware, 150 Academy Street, Newark, Delaware, 19716, USA

† Electronic supplementary information (ESI) available. See DOI: <https://doi.org/10.1039/d4me00177j>



the range of mechanical properties and sensitivity (*i.e.*, the magnitude of their stiffness change) is still limited, hindering their practical use as smart materials.<sup>6–11</sup> Tackling these challenges necessitates new molecular design approaches toward modulating hydrogen bonding arrangements and enhancing our fundamental understanding of the relationship between structural organization and water-adaptive properties.

Currently, a promising strategy towards developing responsive systems with tailorable mechanical performance is to harness self-assembly and non-covalent interactions (*e.g.*, hydrogen bonding) as seen in biological systems.<sup>12</sup> For instance, spider silk exhibits tunable mechanical properties and stimuli-responsiveness because of its self-assembling motifs, which provide a wide array of hydrogen bonding arrangements. Inspired by the hierarchical arrangements in spider silk, self-assembling peptide motifs have been used as building blocks in conventional polymeric materials to tailor microstructure and mechanical properties and to generate responsive behavior.<sup>13–19</sup> Peptides exhibit an array of hierarchical structures and properties *via* modulation of their secondary structures (*e.g.*,  $\alpha$ -helix and  $\beta$ -sheet).<sup>20,21</sup> Natural polypeptides from silk fibroins containing  $\beta$ -sheet crystals were introduced into poly(vinyl alcohol) (PVA) to induce water-responsiveness.<sup>22</sup> In these hybrids,  $\beta$ -sheet crystals served as a “permanent”, crosslinked network that was unaffected by the presence of water, while PVA aided the formation of hydrogen bonds in amorphous regions, which were easily dissociated by water molecules. The introduction of  $\beta$ -sheet crystals enabled a shape change when exposed to water. This research suggests that peptides can serve as an architectural motif to induce water responsiveness in passive materials and can provide an opportunity to tailor responsive properties. Furthermore, peptides have been integrated into polyurethanes/polyureas to broaden their mechanical and stimuli-responsive properties.<sup>17–19</sup> For example, the Hu group employed peptide-containing block copolymers [poly( $\gamma$ -benzyl-L-glutamate)-*b*-poly(propylene glycol)-*b*-poly( $\gamma$ -benzyl-L-glutamate)triblocks] as the soft segment of polyurethanes to develop thermo-responsive materials with high extensibility (>1600%).<sup>19</sup> The Young's modulus and the ability to recover to the original shape increased with increasing peptide content due to the “pseudo” hard segment character of the peptide blocks. As another example, our group utilized a peptide–polyurea platform where poly( $\beta$ -benzyl-L-aspartate)-*b*-poly(dimethylsiloxane)-*b*-poly( $\beta$ -benzyl-L-aspartate) was the soft block in traditional non-chain extended polyureas to investigate the role of peptide secondary structure and hierarchy on thermo-responsive, shape memory behavior.<sup>17</sup> This research demonstrated that an increase in shape memory response (*e.g.*, shape fixity) is driven by a synergistic effect of a phase-separated morphology and peptide secondary conformation. These studies of peptide–polymer hybrids highlight the potential of nature's building blocks to serve as handles to tailor mechanical properties

and heat-triggered responsive behavior. However, the influence of peptidic ordering and hierarchical arrangement on water-responsive mechanics in peptide–polymer hybrids remains an open question.

One pathway toward tailoring water-responsive properties in peptide hybrid materials is to employ co-organization with nanomaterials *via* non-covalent interactions.<sup>23,24</sup> For example, the mechanical properties of silk fibroins were altered through the addition of cellulose nanofibers (CNFs).<sup>25</sup> Strong and selective interfacial interactions between silk fibroins and CNFs led to the formation of “shish kebab”-like hierarchical nanostructures. This interlocked, network morphology contributed to an increase in the Young's modulus (from 8 GPa up to 30 GPa) and strength (from 86 MPa up to 260 MPa). Additionally, these unique nanostructures induced added functionality (*e.g.*, high water flux, water permeation) that highlighted their potential for nanofiltration applications. With this framework, new strategies can be envisioned to tune self-assembly, mechanics, and water-adaptive response *via* nanostructured architectures driven by non-covalent interactions.

Towards the goal of hierarchical, peptide hybrid nanocomposites, we designed a hydrophilic, non-chain extended, poly(ethylene glycol)-based polyurea matrix containing poly( $\beta$ -benzyl-L-aspartate) (PBLA) blocks within the soft segment. The peptide content was modulated to vary hydrogen bonding arrangements in these peptide–polyurea hybrids (PPUs). Cellulose nanocrystals (CNCs) were incorporated into the PPUs to tailor self-assembly and expand their water-responsive behavior. Herein, we aim to elucidate the role of hierarchical architectures in water-triggered mechanical response. This exploration of the interplay between hierarchical architectures and water-induced, mechanically-adaptive properties will provide insight toward the design of next generation responsive materials with environmentally-tunable properties.

## 2. Experimental section

### 2.1. Materials

Anhydrous *N,N*-dimethylacetamide (DMAc, anhydrous, 99.8%, packaged under Argon) was purchased from Fisher Scientific LLC. Tetrahydrofuran (THF, anhydrous, >99.9%) and reagents including  $\beta$ -benzyl-L-aspartate (BLA), triphosgene, 1,6-hexamethylene diisocyanate (HDI), and dibutyltin dilaurate (DBTDL) were obtained from Sigma-Aldrich. All solvents and reagents above were used as received.  $\alpha,\omega$ -Bis(amine)poly(ethylene glycol) (PEG, 2000 g mol<sup>−1</sup>) was purchased from Sinopeg (China) and was dried under vacuum at ~80 °C for 3 hours and then at room temperature for 16 hours prior to use.  $\beta$ -Benzyl-L-aspartate *N*-carboxyanhydride (BLA-NCA) was synthesized according to established literature procedure.<sup>26</sup> TEMPO-cellulose nanocrystals (CNCs) with a carboxyl group content of 2.0 mmol g<sup>−1</sup> were obtained from Cellulose Lab (Canada). These



CNCs had dimensions of 5–20 nm in width and 140–200 nm in length.

## 2.2. Synthesis of poly( $\beta$ -benzyl-L-aspartate)-*b*-poly(ethylene glycol)-*b*-poly( $\beta$ -benzyl-L-aspartate) (PBLA-*b*-PEG-*b*-PBLA)

PBLA-*b*-PEG-*b*-PBLA triblock copolymers were synthesized *via* amine-initiated NCA ring-opening polymerization.<sup>27</sup> The polymerization was conducted in a nitrogen (N<sub>2</sub>) atmosphere glovebox. BLA-NCA (6.1 g, 24 mmol), and a mixture of THF and DMAc in a volumetric ratio of 1:3 (31 mL) was added in an oven dried 100 mL round-bottom flask equipped with a magnetic stirrer and a condenser. To the BLA-NCA solution, 1 g (0.5 mmol) of PEG predissolved in 29 mL of 1:4 THF:DMAc solution was added. The mixture was stirred at room temperature for 24 hours before precipitation into diethyl ether. The precipitate was filtered, washed with diethyl ether three times, and then dried under vacuum until constant weight was obtained.

## 2.3. Synthesis of non-chain extended PBLA-PEG-based polyurea hybrids

Using the PBLA-*b*-PEG-*b*-PBLA triblock as the soft segment, non-chain extended peptidic polyureas (PPUs) were synthesized. For a polyurea control (PEG-HDI PU), only PEG was used as the soft segment. For all samples, an isocyanate/amine ([NCO]:[NH<sub>2</sub>]) ratio of one was used. The desired peptide content was achieved by adding an excess of PEG and modulating the ratio of PBLA-*b*-PEG-*b*-PBLA to PEG in the following eqn (1):<sup>26</sup>

$$\text{wt\% (PBLA)} = 100 \times \left( \frac{xM_{\text{PBLA}}}{xM_{\text{PBLA}} + yM_{\text{PEG}} + zM_{\text{HDI}}} \right) \quad (1)$$

where  $x$ ,  $y$  and  $z$  are the molar quantities of the PBLA, PEG, and HDI, respectively, and  $M_{\text{PBLA}}$ ,  $M_{\text{PEG}}$  and  $M_{\text{HDI}}$  are the molecular weights of PBLA, PEG and HDI, respectively. As reported previously,<sup>26</sup> all non-chain extended PBLA PPUs and the control were synthesized in a nitrogen atmosphere glovebox *via* step-growth (condensation) polymerization. Briefly, the PPU with 20 wt% of PBLA content was synthesized by adding HDI (0.46 g, 2.8 mmol) and 15 mL of 1/2 THF/DMAc to an oven dried 100 mL round bottom flask equipped with a magnetic stirrer and a Virgreux condenser. The triblock (1.84 g, 0.2 mmol) and PEG (5.16 g, 2.6 mmol) were predissolved in 46 mL of 1:3 THF:DMAc solution with 5 drops of DBTDL (catalyst), and then added dropwise to the flask for around 1 hour using a dropping funnel. This solution was stirred for 24 hours at 60 °C and then precipitated into diethyl ether. The precipitate was filtered, washed with diethyl ether three times, and then dried under vacuum until constant weight was obtained (around 2 days).

## 2.4. Preparation of PPU/CNC nanocomposite films

The PPU/CNC nanocomposites were prepared *via* solvent casting and subsequent thermal treatment. First, PPUs were dissolved in 1:3 THF:DMAc at a concentration of 50 mg

ml<sup>-1</sup> by overnight stirring at room temperature. Next, the aqueous CNC dispersions were re-dispersed in DMAc *via* a solvent-exchange process.<sup>11,28,29</sup> The PPU/CNC nanocomposite films containing 10 wt% of CNCs were prepared by adding CNCs into the polymer solutions. These mixtures were stirred overnight and cast into Teflon dishes. The dishes were placed in a hood for around 10 days to evaporate the solvent, and then placed in a vacuum oven at 60 °C (above the PEG melting point) for 1 day and at room temperature for 2 days to remove any residual solvent and obtain the equilibrium nanostructures. The neat PPU and control films were prepared similarly. The average thickness of the dried films was ~0.15 mm.

## 2.5. Molecular weight characterization

<sup>1</sup>H nuclear magnetic resonance (<sup>1</sup>H NMR) spectrum of PBLA-*b*-PEG-*b*-PBLA triblock was recorded on a Bruker 600 MHz spectrometer using DMSO-*d*<sub>6</sub>;  $\delta$  2.5 as the solvent, and the block length of PBLA in the PBLA-*b*-PEG-*b*-PBLA was calculated using end-group analysis:  $\delta$  = 7.3 ppm (H<sub>arom</sub>), 5.7–5.2 ppm (H<sub>benzyl</sub>), 4.6 ppm ( $\alpha$ -CH<sub>2</sub>-), 3.9 ppm (188H, CH<sub>2</sub>-CH<sub>2</sub>O), 3.1 ppm ( $\beta$ -CH<sub>2</sub>-).

To characterize the number-average molecular weight ( $M_n$ ) and dispersity ( $D = M_w/M_n$ ) of neat PPU samples, gel permeation chromatography (GPC) measurements were performed on a TOSOH Bioscience EcoSEC Elite system equipped with TSKgel columns (three SuperH and one SuperAW5000 columns) and a refractive index (RI) detector. DMAc with 0.5 wt% lithium bromide (LiBr) was used as the eluent at a flow rate of 0.4 mL min<sup>-1</sup> at column temperature of 50 °C. A calibration curve was obtained using six poly(methyl methacrylate) (PMMA) standards (4760 g mol<sup>-1</sup>; 9150 g mol<sup>-1</sup>; 30 780 g mol<sup>-1</sup>; 146 500 g mol<sup>-1</sup>; 260 900 g mol<sup>-1</sup>; 675 500 g mol<sup>-1</sup>). PMMA standards were used instead of PEG standards due to the limited solubility of higher molecular weight PEG (~30 000 g mol<sup>-1</sup>) in this GPC solvent system.

## 2.6. Attenuated total reflection – Fourier transform infrared spectroscopy (ATR-FTIR)

ATR-FTIR spectra were obtained using a Thermo Nicolet NEXUS 470 FTIR spectrometer with a Smart Orbit Diamond ATR accessory. All spectra of the dried films were collected averaging 128 scans with a resolution of 4 cm<sup>-1</sup> in the range of 400–4000 cm<sup>-1</sup>. To determine the secondary structures in each resultant film, the acquired ATR-FTIR spectra were analyzed in the amide I region (1700–1600 cm<sup>-1</sup>). The spectra were baseline-corrected to eliminate background noise. Then, characteristic absorption peaks corresponding to the  $\alpha$ -helix and  $\beta$ -sheet structures were identified *via* second derivative analysis, which aids in resolving overlapping peaks in the amide I band and improving the precision of peak identification. A peak appearing at 1620–1645 cm<sup>-1</sup> was indicative of  $\beta$ -sheets, whereas a peak at 1650–1660 cm<sup>-1</sup> was assigned to  $\alpha$ -helices. To quantify the fraction of each



secondary structure, the amide I band was deconvoluted into Gaussian curves using Origin Lab software. The relative fraction of  $\alpha$ -helices to  $\beta$ -sheets was calculated using the following eqn (2):

$$\frac{A_{1650-1660\text{cm}^{-1}}}{A_{1620-1645\text{cm}^{-1}} + A_{1650-1660\text{cm}^{-1}}} \times 100(\%) \quad (2)$$

where  $A_{1620-1645\text{cm}^{-1}}$  and  $A_{1650-1660\text{cm}^{-1}}$  indicate the integral areas under the peaks in the ranges of  $1620-1645\text{ cm}^{-1}$  and  $1650-1660\text{ cm}^{-1}$ , respectively.

## 2.7. Differential scanning calorimetry (DSC)

DSC experiments were performed on a TA instruments Discovery series calorimeter. The dried films were tested at a heating rate of  $10\text{ }^{\circ}\text{C min}^{-1}$  over the temperature range of  $-80$  to  $160\text{ }^{\circ}\text{C}$  under a  $\text{N}_2$  atmosphere. The degree of crystallinity was calculated by dividing the melting enthalpy of each sample by the enthalpy of melting required for a 100% crystalline PEG sample ( $\Delta H_0 = 196.8\text{ J g}^{-1}$ ).<sup>27</sup>

## 2.8. Wide-angle X-ray scattering (WAXS) and small-angle X-ray scattering (SAXS)

WAXS and SAXS data were collected using a Xenocs Xeuss 2.0 type of instrument. X-ray were generated at  $50\text{ kV}/0.6\text{ mA}$  at a beam wavelength of  $1.542\text{ \AA}$  ( $\text{Cu K}\alpha$  radiation). A sample-to-detector distance was adjusted to  $72$  and  $550-1200\text{ mm}$  for the WAXS and SAXS measurements, respectively. The scattered beam was recorded on a CCD detector with a pixel resolution of  $172 \times 172\text{ }\mu\text{m}$ . The scattering patterns of dried films were recorded over  $15$  minutes of exposure time at room temperature. Using Foxtrot 3.4.9., 2D patterns were azimuthally integrated to obtain the scattering intensity as a function of scattering vector,  $q$ , where  $q = 4\pi \sin(\theta)/\lambda$  and  $2\theta$  is the scattering angle. Origin 9.6 was utilized for data processing.

## 2.9. Atomic force microscopy (AFM)

The AFM images of dried films were taken on a Bruker Multimode in tapping mode in air. Bruker antimony doped silicon tips ( $320\text{ kHz}$ ,  $125\text{ }\mu\text{m}$ ) were used.  $1\text{ }\mu\text{m} \times 1\text{ }\mu\text{m}$  and  $2\text{ }\mu\text{m} \times 2\text{ }\mu\text{m}$  images were collected with  $256$  scans per line at a frequency of  $1\text{ Hz}$ . All images were processed using the Bruker Nanoscope Analysis 1.5 software.

## 2.10. Tensile testing

Tensile testing was conducted on a Zwick mechanical testing instrument equipped with a  $100\text{ N}$  load cell. For the testing, all dried films were cut into a dog bone shape according to a modified ASTM D1708 with the dimensions scaled down by a factor of  $2$ . All samples were elongated to failure at room temperature in constant strain mode with a strain rate of  $100\%$  of the initial gauge length per minute. Mechanical properties and stress-strain curves were averaged from at least three sample measurements.

## 2.11. Swelling behavior

Prior to dynamic mechanical analysis (DMA) testing, the degree of aqueous swelling of the dried films was calculated gravimetrically by measuring their weight before and after immersion in deionized water (DI water) at room temperature for  $24\text{ h}$  and using the following eqn (3):<sup>11</sup>

$$\frac{\text{weight of wet sample} - \text{weight of dry sample}}{\text{weight of dry sample}} \times 100\% \quad (3)$$

To minimize the error in measuring the swelling ratio, the wet samples were placed on a filter paper to wick the water from the surface of the swollen samples before weighing.

## 2.12. DMA

The water-responsive mechanical properties of all dried samples were determined using an RSA-G2 solid analyzer (TA Instrument) equipped with a submersion chamber that enabled measuring of the storage modulus while the films were immersed in DI water. All samples were dried under vacuum at room temperature prior to DMA testing. Tests were conducted in tensile mode using with a strain of  $0.2\%$  and a fixed frequency of  $1\text{ Hz}$  under isothermal conditions at room temperature ( $21-24\text{ }^{\circ}\text{C}$ ). Also, all tests were performed in triplicate and error bars were plotted to indicate standard deviations.

# 3. Results and discussion

## 3.1. Molecular design for water-responsive PPU/CNC nanocomposites

In this research, the influence of hierarchical arrangements on the water-responsive mechanical properties of polyureas was investigated *via* two pathways: 1) the incorporation of peptide motifs into a water-soluble PEG-based polyurea, yielding PPUs, and 2) the addition of cellulose nanocrystals into the series of PPU matrices.

Specifically, we used peptide-based triblocks (ABA-type triblocks) as the soft segment of non-chain extended polyureas (Fig. 1), where A refers to a PBLA peptide block and B is a semi-crystalline PEG. The  $^1\text{H}$  nuclear magnetic resonance ( $^1\text{H NMR}$ ) spectrum of the triblock confirmed the average PBLA repeat length of  $\sim 21$  (Fig. S1†). For the hard segment, HDI was employed without a chain extender. The non-chain extended polyureas were chosen to mitigate the impact of the hard domain on the water-responsive behavior so that the soft segment arrangements can be considered as the primary factor affecting the microphase-separated morphology and properties of PPUs. Also, water-soluble PEG-based polyurea was used to examine the role of peptidic ordering on water-responsive properties. The PBLA weight fraction was controlled to probe the relationship between hierarchical ordering and water-triggered storage modulus changes in the neat PPUs. Moreover,  $10\text{ wt}\%$  of CNCs were incorporated into the PPU matrices to investigate the impact of matrix-filler (PPU-CNC) interactions on the hierarchical





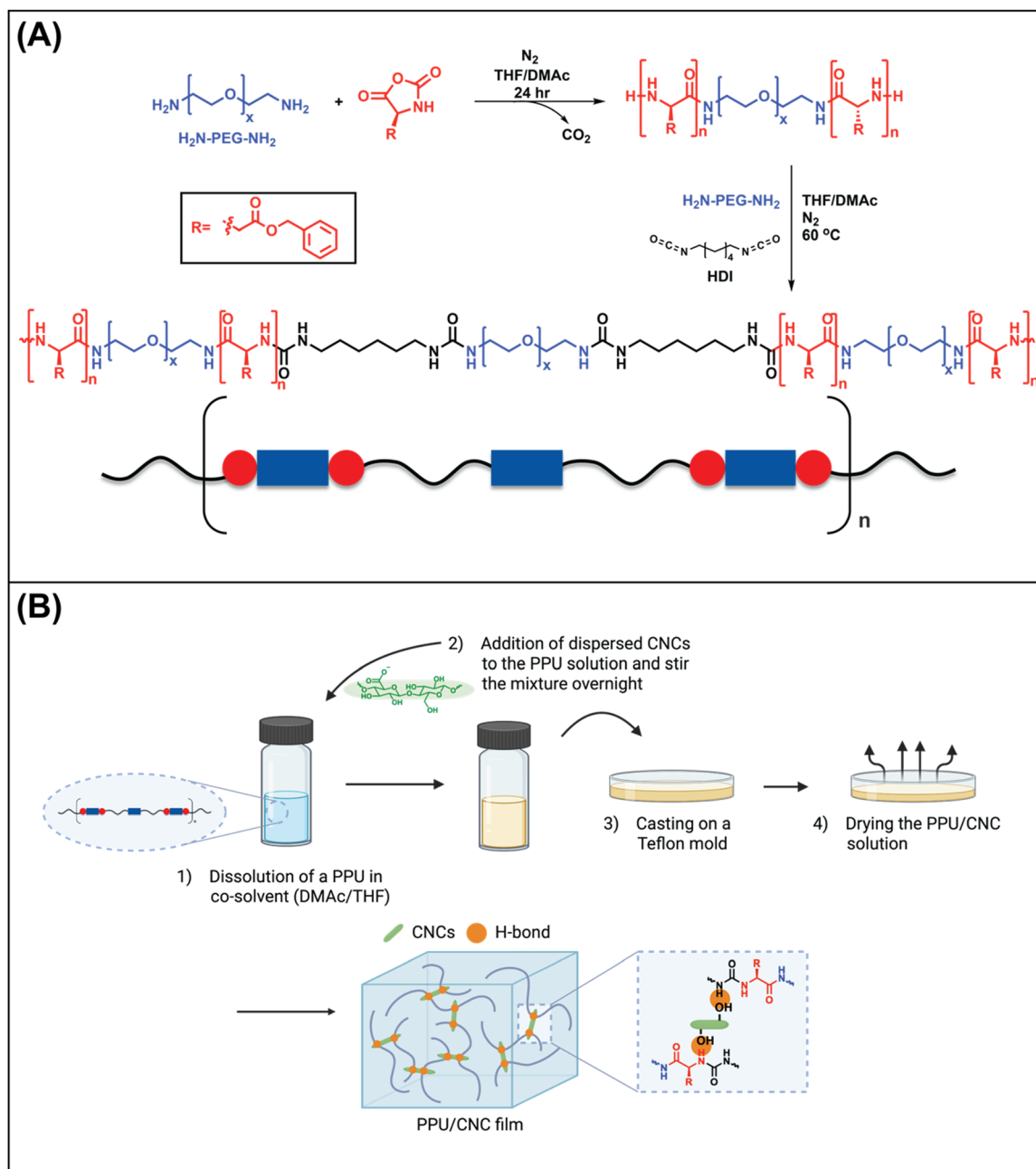


**Fig. 1** (A) Overview of the PPU synthesis process, which is utilized as the matrix material in our nanocomposite system. (B) Step-by-step illustration for the preparation of the PPU/CNC nanocomposite film, highlighting the formation of hydrogen bonding interactions between the PPU and CNCs.

organization and mechanical response of PPU/CNC nanocomposites. For the nomenclature,  $An-X$  was used for the PPUs and  $An-X/CNCY$  was employed for the PPU/CNC nanocomposites, where  $A$  indicates non-chain extended peptide–polyurea hybrids consisting of PBLA- $b$ -PEG- $b$ -PBLA as the soft segment,  $n$  is the peptide repeat length (21),  $X$  is the peptide weight fraction in the resultant sample (20 or 40 wt%), and  $Y$  is CNC content (in wt%). The control film without PBLA was denoted as PEG–HDI PU. The molecular weight and dispersity of the series of PPUs and the control are listed in Fig. S2.†

### 3.2. Characterization of hydrogen bonding arrangements: peptide secondary structure and matrix–filler interactions

To examine the PBLA secondary structures present in all dried films, ATR-FTIR analysis was conducted. Specifically, the amide I band ( $1600\text{--}1700\text{ cm}^{-1}$ ; associated mainly with carbonyl ( $\text{C=O}$ ) stretching) was utilized to identify the peptide secondary structure due to its sensitivity to peptide conformation and hydrogen bond patterns.<sup>30</sup>  $\beta$ -sheets and  $\alpha$ -helices are stabilized through inter- and intra-molecular hydrogen bonding, respectively.  $\beta$ -sheets appear between



1620 and 1645  $\text{cm}^{-1}$ , whereas  $\alpha$ -helices exhibit an absorption band at 1650–1660  $\text{cm}^{-1}$ .<sup>31,32</sup> Fig. 2 shows that all neat PPU (A21–20 and A21–40) exhibit two distinct peaks at 1633 and 1659  $\text{cm}^{-1}$ , indicating the presence of both  $\beta$ -sheets and  $\alpha$ -helices. The intensity of the two peaks was modulated with increasing PBLA content, which is indicative of an increased PBLA volume density. The relative fraction of  $\alpha$ -helices to  $\beta$ -sheets in A21–20 and A21–40 was 0.51 and 0.48, respectively. The ratio of  $\beta$ -sheet to  $\alpha$ -helical content remained  $\sim 50/50$  although the PBLA content increases. This trend is different from our previous investigation where poly( $\epsilon$ -carbobenzoyloxy-L-lysine)-*n*-*b*-poly(ethylene glycol)-*b*-poly( $\epsilon$ -carbobenzoyloxy-L-lysine) (PZLL-*b*-PEG-*b*-PZLL) was used as a soft segment.<sup>27</sup> In these peptide-polyurea hybrids, the  $\alpha$ -helix content was 58% at 20 wt% of the overall peptide weight fraction, and the  $\alpha$ -helical conformation dominated with increasing peptide content to 40 and 60 wt%. The secondary structure in peptide-containing block copolymers is generally influenced by several factors: 1) the chemical structure of the peptide segment, 2) the volume fraction of each block, and 3) the structure, polarity, and molecular weight of the adjacent polymer block.<sup>17,31,33,34</sup> Unlike PZLL, which predominantly forms  $\alpha$ -helical conformations, PBLA tends to adopt both  $\alpha$ -helical and  $\beta$ -sheet structures.<sup>27</sup> The benzyl ester side groups in PBLA introduce additional hydrophobicity compared to PZLL, which significantly affects its self-assembly behavior. The propensity of PBLA to form  $\beta$ -sheet structures and its preference for intermolecular hydrogen bonding in these PPU systems also may be attributed to the lower PEG molecular weight ( $\sim 2000 \text{ g mol}^{-1}$ ). Lower molecular weight PEG is less readily crystallized, promoting greater phase mixing between the PEG and PBLA segments compared to analogous PPUs with a higher PEG molecular weight.<sup>35</sup> This enhanced phase mixing facilitates the

formation of  $\beta$ -sheets and intermolecular hydrogen bonding in PBLA.

The addition of 10 wt% CNCs to A21–20 caused the absorption peaks at 1633 and 1659  $\text{cm}^{-1}$  to weaken and broaden (Fig. 2), indicating disruptions in the organization of the PBLA segments. A similar trend was observed for A21–40/CNC10. These findings suggest that the presence of CNCs introduces new hydrogen bonding interactions (Fig. 1B) that compete with PBLA–PBLA hydrogen bonding, disrupting PBLA segment organization. Overall, the ATR-FTIR results reveal that hydrogen bonding arrangements can be readily varied through altering peptide structure and content, and promoting peptide–CNC interactions. This flexibility in peptide-based systems allows fine-tuning of molecular interactions, influencing phase separation, ordering, and morphology—key factors in mechanical and stimuli-responsive properties.<sup>17,27,36</sup> Further details on hierarchical organization are discussed in section 3.3.

### 3.3. Identifying structural organization across multiple length scales

DSC was used to explore the influence of physical associations on the phase separation behavior of PPUs and PPU/CNC nanocomposites. First heating and cooling curves of all dried samples are shown in Fig. 3A, and the analyzed DSC data are summarized in Fig. 3C. The PEG homopolymer ( $\sim 2000 \text{ g mol}^{-1}$ ) typically undergoes melting at around 50  $^{\circ}\text{C}$  and crystallization at 20–30  $^{\circ}\text{C}$ .<sup>37,38</sup> The control, non-chain extended PEG–HDI polyureas displayed a PEG melting temperature ( $T_m$ ) at 42–45  $^{\circ}\text{C}$  with a percent crystallinity of 40%. This crystallinity is considerably lower than in PEG–HDI polyureas (86%) with a higher molecular weight PEG segment ( $3400 \text{ g mol}^{-1}$ ), which was previously reported.<sup>27</sup> Similarly, in chain-extended poly(ethylene oxide) (PEO)-based polyurethanes, a decreased soft segment (PEO) molecular weight resulted in a less pronounced melting transition and a lower crystallinity within the soft phase because the shorter PEO block tends to crystallize less in the segmented polyurethanes.<sup>35</sup> It also is important to highlight that the PEG-based polyurea control exhibited an absence of hard segment melting temperature, which is likely a result of extensive associations between the PEG and hard blocks (urea linkages).<sup>39</sup> This observation is in contrast to non-chain extended polyureas consisting of poly(dimethyl siloxane) (PDMS), which underwent a hard segment melting transition at around 85–90  $^{\circ}\text{C}$  due to incompatibility between the PDMS blocks and urea linkages.<sup>17</sup>

The introduction of the PBLA block reduced the  $T_m$  to  $\sim 40$   $^{\circ}\text{C}$  and the PEG crystallinity below 30%, indicating that the PBLA segment hinders PEG crystallization. As the PBLA content increases from 20 to 40 wt%, the crystallinity was gradually reduced from 28% to 21%, but the  $T_m$  was essentially constant ( $\sim 40$   $^{\circ}\text{C}$ ). The reduction of PEG crystallinity with increasing PBLA weight fraction implies an

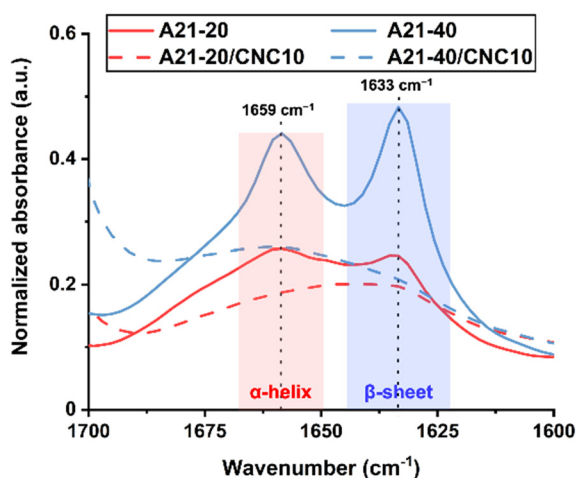
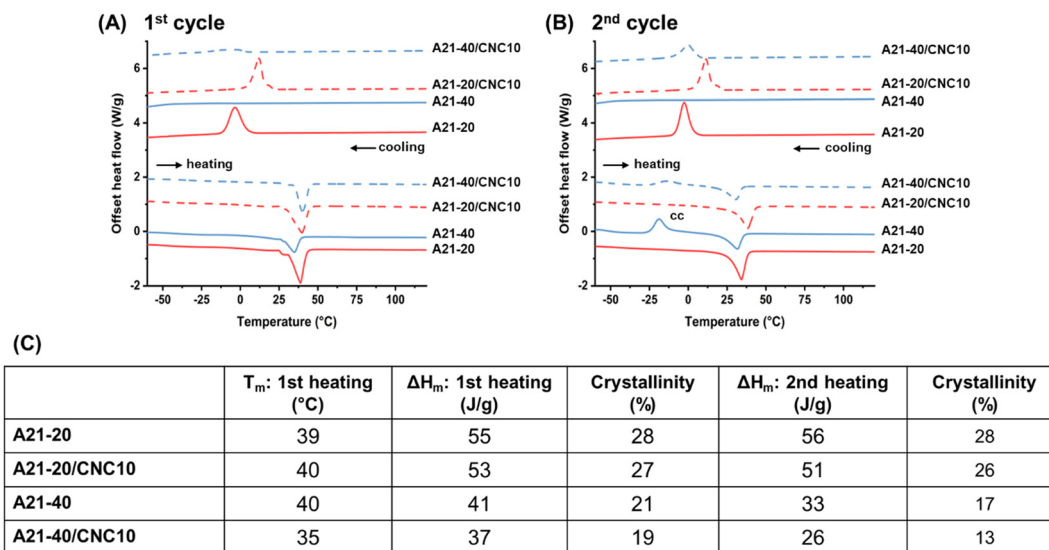


Fig. 2 ATR-FTIR spectra of PPUs (solid lines) and PPU/CNC nanocomposites (dash lines) in the amide I region (1700–1600  $\text{cm}^{-1}$ ) to identify peptidic ordering with varying the PBLA and CNC content.





**Fig. 3** DSC thermograms of PPUs and PPU/CNC nanocomposites during (A) first heating and cooling cycles and during (B) second heating and cooling cycles. (C) Table summarizing the DSC analysis results: the PEG melting temperature ( $T_m$ ) and PEG percent crystallinity ( $\Delta H_m/\Delta H_0$  where  $\Delta H_m$  is the enthalpy of fusion of the PEG segment and  $\Delta H_0$  is the enthalpy of fusion of a 100% crystalline PEG, which is  $196.8 \text{ J g}^{-1}$ ).<sup>27</sup> In the second heating cycles, cc indicates cold crystallization.

increase in phase mixing through hydrogen bonding interactions between the PBLA and PEG blocks.<sup>27,40</sup> As we speculated in the ATR-FTIR analysis, the shorter PEG block and higher PBLA content can lower PEG crystallinity and induce the increased associations between the soft segments, which may hinder the formation of  $\alpha$ -helical structures and promote inter-molecular hydrogen bonding arrangements.

Interestingly, in the first cooling curve (Fig. 3A), the PEG crystallization temperature ( $T_c$ ) disappeared and a glass transition began to emerge below  $-50^\circ\text{C}$  with increasing PBLA content from 20 to 40 wt%, indicating that the re-formation of the crystalline PEG domain is prevented at the higher PBLA fraction.<sup>28</sup> Furthermore, in the second heating curve (Fig. 3B), the glass transition ( $-52^\circ\text{C}$ ) and subsequent PEG cold crystallization ( $T_c = -19^\circ\text{C}$ ) were observed only in A21-40. Cold crystallization occurs below  $T_m$  when supercooled molecules that are not crystallized and exist in a frozen amorphous state begin to form crystal nuclei as temperature increases above  $T_g$ .<sup>41</sup> Polymeric materials exhibiting cold crystallization generally tend to have a slow rate of crystallization.<sup>42</sup> Unlike the A21-40, the cold crystallization behavior was not seen in PPUs with a longer PEG soft segment ( $3400 \text{ g mol}^{-1}$ ) and 40 wt% of peptide (poly( $\epsilon$ -carbobenzoyloxy-L-lysine)).<sup>27</sup> The shorter PEG segment ( $2000 \text{ g mol}^{-1}$ ) used in this investigation can facilitate phase mixing between the PEG and PBLA blocks and reduce the rate of crystallization, hindering the PEG crystallization at the cooling rate of  $10^\circ\text{C min}^{-1}$  and subsequently leading to an amorphous soft phase. It is worth noting that the thermal treatment (*i.e.*, drying at  $60^\circ\text{C}$ ) suppresses the cold crystallization as depicted in the first heating curve, indicating that a relatively slow cooling enables PEG crystallization.<sup>43</sup> Thus, this further examination of DSC data

supports the assertion that the molecular weight of the PEG block and the peptide content have a significant impact on PEG crystallization and phase separation.

Upon 10 wt% CNC loading into A21-20, the  $T_m$  and PEG crystallinity remained relatively constant (Fig. 3A), suggesting that the CNCs have limited interactions with the PEG segment.<sup>44</sup> In contrast, CNC incorporation into A21-40 reduced the  $T_m$  to  $35^\circ\text{C}$  from  $40^\circ\text{C}$  with a slight decrease in the enthalpy of fusion ( $\Delta H_m$ ) of the PEG segment and the PEG percent crystallinity due in part to moderate interactions between the PEG and CNCs.<sup>28</sup> The first cooling cycles (Fig. 3A) highlight that CNC incorporation significantly varied the PEG crystallization behavior. For A21-20/CNC10 composites, the  $T_c$  considerably increased to  $12^\circ\text{C}$  from  $-4^\circ\text{C}$  for the neat A21-20. In A21-40/CNC10 composites, the crystallization peak appeared at  $\sim -4^\circ\text{C}$ , in contrast to the pure A21-40 in which  $T_c$  is absent. The earlier onset of PEG crystallization and the appearance of a crystallization peak suggest that the CNCs act as nucleating agents in the PPU/CNC nanocomposites, which also was observed in conventional cellulose-reinforced polymers.<sup>44,45</sup> Additionally, a smaller cold crystallization peak was observed in the second heating curve of A21-40/CNC10 compared to the second heating curve of A21-40 (Fig. 3B) as a result of the CNC nucleation.<sup>46</sup> Overall, the DSC results illustrate that increasing PBLA content in neat PPUs induces more phase mixing and diminishes PEG crystallinity, whereas the presence of CNCs in PPUs minimally impacts the PEG crystallinity due to modest PEG-CNC interactions.

While the DSC data provide indirect information on structural variations upon PBLA and CNC incorporation into non-chain extended PEG-based polyureas, WAXS is a powerful tool to elucidate the crystal structure of the PEG





block and peptide secondary structures. As seen in Fig. 4A, intense and sharp diffraction peaks arose at  $2\theta = 19.2^\circ$  (0.46 nm) and  $23.4^\circ$  (0.38 nm), corresponding to (120) and (032) crystal plane reflections of PEG crystallites.<sup>47–49</sup> This observation suggests that PEG chains are crystallized in the PPUs, which is consistent with the DSC results. As the PBLA content varied from 20 to 40 wt%, the PEG crystalline peak intensities were reduced, indicating that a higher PBLA content leads to a decrease in the PEG crystallinity due in part to increased physical associations between PBLA and PEG segments or increased phase mixing.<sup>27,31</sup> CNC addition into PPU

matrices did not alter the PEG crystalline peak positions and intensities, indicating that CNC incorporation does not change the crystal structure of PEG. The PEG crystallization behavior from WAXS as a function of PBLA and CNC content agrees well with the DSC analysis.

Probing reflections at lower scattering angles in WAXS provides information on secondary conformations present in the neat PPUs and PPU/CNC nanocomposites. For peptide-containing materials, the reflection peak at  $\sim 4.9^\circ$  ( $q = 3.48 \text{ nm}^{-1}$ , a distance of 1.80 nm) is assigned to the distance between backbones in the antiparallel, intermolecular hydrogen-bonded  $\beta$ -sheets, while the peak at  $\sim 6^\circ$  ( $q = 4.37$

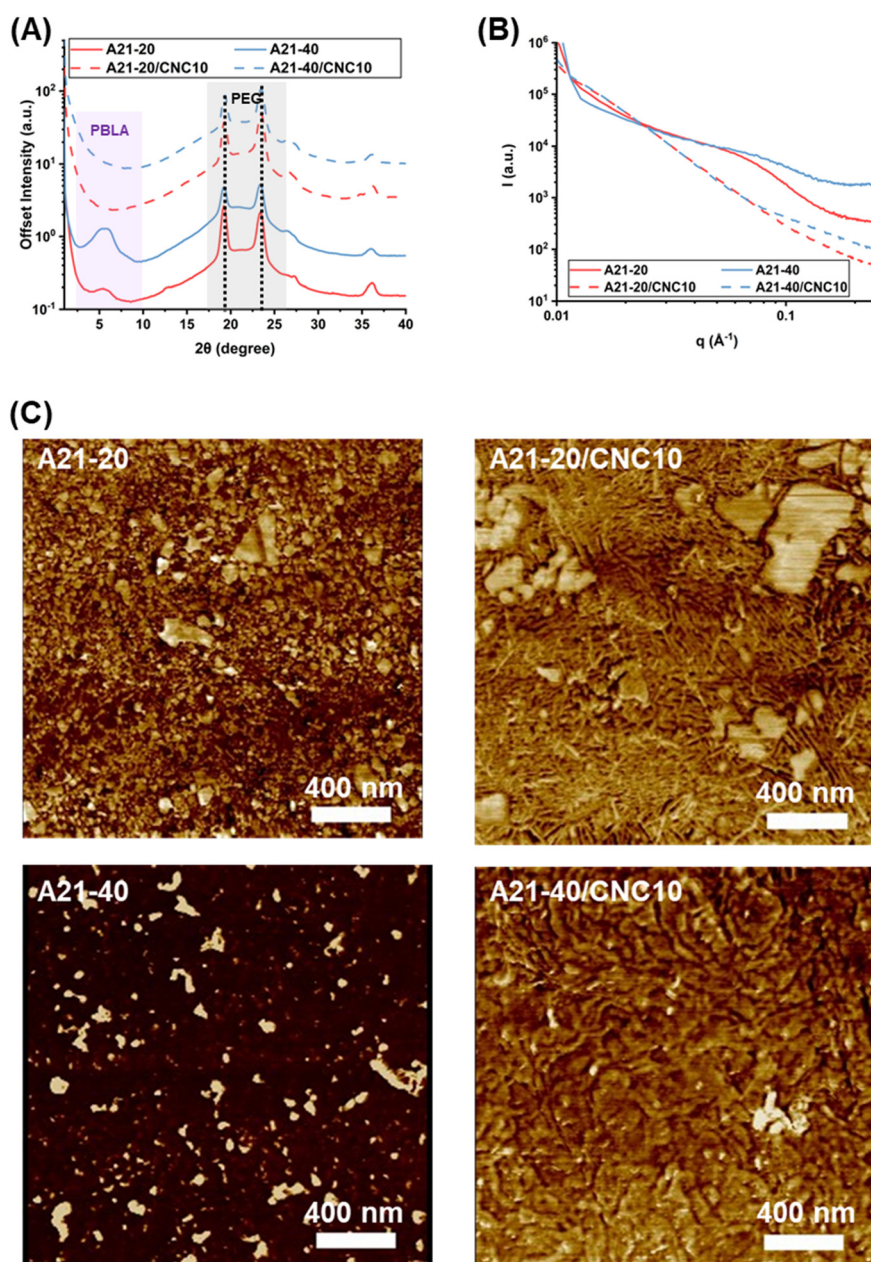


**Fig. 4** Characterization of hierarchical structures of PPUs and PPU/CNC nanocomposites from nano- to micro-scale: (A) WAXS data probing the crystallization behavior of the soft phase (*i.e.*, PBLA and PEG segments). (B) 1-D SAXS profiles of PPU and PPU/CNC films with varying PBLA and CNC content. (C) AFM phase images of the surface of dried PPU and PPU/CNC nanocomposite films ( $2 \times 2 \mu\text{m}$ ).





nm<sup>-1</sup>, a distance of 1.47 nm) is indicative of  $\alpha$ -helical arrangements.<sup>50</sup> For all of the neat PPU samples, a broad reflection peak appeared in the region of  $2\theta = 4.0$ – $8.0^\circ$  (Fig. 4A). The appearance of this broad peak may result from the overlap of  $\beta$ -sheet and  $\alpha$ -helix reflections, supporting the existence of a mixture of  $\beta$ -sheets and  $\alpha$ -helices as observed in the ATR-FTIR spectra (Fig. 2). The peak intensity increased with increasing PBLA content, indicating enhanced peptidic organization within the soft phase. In the neat PPUs, the emergence of PEG and PBLA crystalline diffraction peaks indicates that PBLA domains are not completely compatible with PEG domains and all PPU samples exhibit some degree of phase segregation.<sup>31,51</sup> Interestingly, in the composite films (A21–20/CNC10 and A21–40/CNC10), the reflection peaks related to  $\alpha$ -helices and  $\beta$ -sheets disappeared, signifying the disruption of peptidic ordering as a result of extensive PBLA–CNC interactions. This finding agrees well with the ATR-FTIR results (Fig. 2). Thus, the WAXS results reveal that: 1) the neat PPUs exhibit both PEG crystallinity and PBLA ordering, and 2) the CNCs preferentially interact with the PBLA blocks compared to the PEG segments in the PPU/CNC composites, reducing peptidic ordering.

While the WAXS studies revealed the molecular organization at the angstrom scale, SAXS experiments were carried out to explore the nanometer-scale organization of the PPU/CNC composites. SAXS is widely used to evaluate the domain spacing and the degree of phase separation in polymeric materials.<sup>52–54</sup> A two-phase model is typically adopted to interpret the SAXS data of traditional segmented polyureas and polyurethanes, involving ordered hard and amorphous soft phases.<sup>55</sup> On the basis of ATR-FTIR, DSC, and WAXS results, PPUs are better represented by a pseudo three-phase system comprised of crystalline PEG domains, ordered peptidic domains, and mixed phases (*i.e.*, the hard segments hydrogen bonded with the soft segments). Furthermore, the peptide block itself has the ability to display long-range ordering and microstructure *via* physical interactions, such as hydrogen bonding and  $\pi$ – $\pi$  stacking.<sup>56</sup> As a route to analyzing the SAXS data of PPUs, the rigid PBLA block was considered as a part of the hard domain, and thus, the  $d$ -spacing in this system indicates the spacing of “pseudo” hard domain.<sup>57</sup> The inter-domain spacing ( $L = 2\pi/q$ ) was calculated using Lorentz-corrected SAXS curves.<sup>55,58,59</sup> As illustrated in Fig. 4B, A21–20 and A21–40 displayed a single, broad peak at  $q \sim 0.7 \text{ nm}^{-1}$  ( $L \sim 9 \text{ nm}$ ), denoting microphase segregation and long-range ordering. Increasing PBLA loading resulted in peak broadening, which provides evidence of a wider distribution of pseudo hard domains or a more phase-mixed morphology in the A21–40 film compared to the A21–20 film.<sup>40,59</sup> Upon CNC loading, the reflection peak of the A21–20 and A21–40 nanocomposites disappeared, which was attributed to a reduction in the regularity of the nanodomain and/or a larger domain size exceeding the detector limit.<sup>31,55,57</sup> These SAXS results reveal that the existence of peptidic ordering in PPUs leads to hierarchical assembly, while the occurrence of PBLA–

CNC interactions in PPU/CNC composites causes shifts in structural organization.

To visualize and assess the microphase-separated morphology, AFM was employed. The morphology of polyurea and polyurethane materials generally depends on hydrogen bonding organization within the soft and hard blocks and the degree of incompatibility between soft and hard blocks.<sup>59</sup> Fig. 4C displays phase images of dried PPU and PPU/CNC films where brighter regions (higher modulus) correspond to crystalline domains and CNC particles, and darker areas (lower modulus) represent the amorphous phase.

The neat PPUs exhibited droplet-like hard domains that are randomly dispersed in a continuous soft phase. In A21–20, some droplets with irregular sizes were interconnected with short rods (indicated by yellow circles in Fig. S3†). For A21–40, discontinuous, bright spots (islands) were dispersed in the continuous soft phase. Furthermore, the increase in PBLA content yielded a dominant soft phase (*i.e.*, larger dark areas than bright areas), which may be driven by variations in the hydrogen bonding arrangements (Fig. 2) and the degree of phase separation (Fig. 3, 4A, and B).<sup>60–62</sup> The morphologies observed in these PPUs are in contrast to traditional polyurea and peptide–polyurea systems where rod/ribbon-like morphologies were formed as a result of the self-assembly of hard or pseudo hard (hard and peptide) segments.<sup>17</sup> This discrepancy can be attributed to the lack of well-defined hard domains *via* extensive hydrogen bonding between the soft and hard segments and phase mixing within the soft segment through PBLA–PEG interactions in the PPUs. This outcome supports the importance of the extent of interactions within a soft segment and/or between soft and hard segments on the morphology of hybrid materials.

A different morphological landscape emerged upon CNC incorporation into the PPU matrices due to the replacement of PBLA–PBLA interactions by PBLA–CNC hydrogen bonding (Fig. 2). At the lower peptide content (20 wt%), the PPU/CNC composites exhibited irregular droplets/platelets and interlocking nanorods ( $\sim 10 \text{ nm}$  in width) (Fig. 4C and S3†). Interestingly, “shish kebab”-like nanostructures appeared in A21–20/CNC10 (indicated by yellow circles in Fig. S3†). Similar morphologies were reported in silk fibroin/cellulose nanofiber nanocomposites, stemming from the preferential organization of the crystalline and amorphous domains of the silk along the cellulose *via* their physical associations and axial distribution of crystalline planes.<sup>25</sup> In contrast, the PPU/CNC nanocomposites with the higher peptide content (40 wt%) formed ripple-like structures, which also is likely as a consequence of the self-assembly of the matrix along CNC nanorods. Thus, matrix–filler associations led to hierarchical structural transitions. Similarly, morphological shifts upon CNC addition were reported in other polymer/cellulose nanocomposites where interactions between polymer matrices and cellulose are responsible for the microstructure of composites.<sup>60,63</sup> Thus, the AFM images illustrate that the self-assembled morphology in this material platform highly

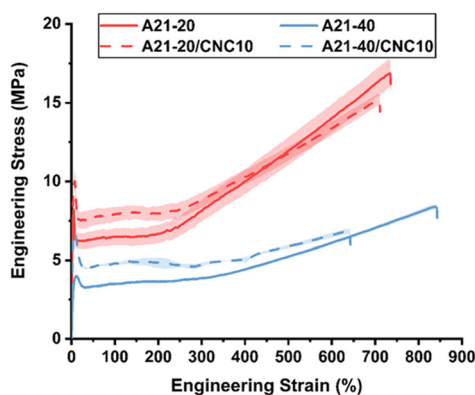


depends on hydrogen bonding arrangements influenced by peptidic ordering and matrix–filler interactions. In the following sections, how these variations in hierarchical organization influence the mechanical response are highlighted.

### 3.4. Elucidating relationships between hydrogen bonding arrangements and tensile mechanical properties in PPU and PPU/CNC nanocomposites

The impact of hierarchical structures on the mechanical properties of PPUs and PPU/CNC nanocomposites was explored *via* tensile testing at room temperature, which is between the PEG  $T_g$  and  $T_m$  of all dried films. Hydrogen bonding arrangements play a critical role in the mechanical behavior of polymeric materials.<sup>64</sup> On the basis of previous studies of polyurethane-based material systems,<sup>27,34,65,66</sup> it was expected that three major factors would determine the mechanical properties of a series of PEG-based PPUs and their nanocomposites: 1) soft segment ordering driven by PEG crystallinity and peptide secondary structure, 2) matrix–filler and/or filler–filler interactions induced by CNC incorporation, and 3) the microphase-separated morphology of resultant materials. Fig. 5 displays the stress–strain curves and details the tensile properties, including Young's modulus, yield strength, strain-at-break, and toughness, of all the samples. All PPUs and PPU/CNC nanocomposites underwent elastic deformation, yielding, necking, and strain hardening (*i.e.*, increasing stress during deformation), which is indicative of well-ordered structures in the resultant samples.<sup>67</sup> Specifically, under tensile stress, the elastic

amorphous component first undergoes deformation, followed by yielding and necking of spherulites and crystal lamellae, and finally strain hardening up to failure as a result of large scale orientation of chain molecules and lamellar crystals.<sup>67</sup> For the neat PPUs, the higher PBLA content slightly increased elongation but diminished Young's modulus, yield strength, and toughness, which can be ascribed to the lower PEG crystallinity and the increased phase mixing between PEG and PBLA segments. A similar argument was reported in PEO-containing polyurethane and peptide–polyurea systems where a phase mixed morphology led to a lower yield strength.<sup>27,66,67</sup> These previous studies also proposed that PEO crystallites contribute to an enhancement in stiffness and toughness by serving as a load-bearing phase. This load-bearing behavior was more apparent in A21–20 with the higher PEG crystallinity compared with the A21–40, evidenced by a strong tendency to neck during the deformation process and less extensibility. The PPU/CNC nanocomposites (Fig. 5) exhibited a higher Young's modulus compared to the corresponding PPU matrices, although the PEG crystallinity remained relatively unchanged upon CNC incorporation (Fig. 3 and 4A). This observed behavior may stem from their morphological shifts to either interlocking or interconnected structures (Fig. 4C and S3†) driven by additional filler–filler interactions and/or variations in hydrogen bonding arrangements from PBLA–PBLA to PBLA–CNC associations (Fig. 2 and 4A). Moreover, the nucleation effect of CNCs (Fig. 3) can facilitate the formation of more compact interconnected nanostructures.<sup>44</sup> The elongation-at-failure of PPU/CNC composites decreased compared to the neat PPUs.



	Young's modulus (MPa)	Yield strength (MPa)	Strain-at-failure (%)	Toughness (MJ/m <sup>3</sup> )
A21-20	311 ± 55	8 ± 1	756 ± 18	77 ± 7
A21-20/CNC10	397 ± 13	10 ± 1	738 ± 47	78 ± 13
A21-40	95 ± 11	4 ± 0.3	886 ± 52	47 ± 6
A21-40/CNC10	276 ± 39	7 ± 0.5	676 ± 47	35 ± 4

Fig. 5 Averaged stress–strain curves of dried PPU and PPU/CNC films (the shaded area around each curve represents the error bars, indicating the variability from the average values calculated from three independent tests). Table summarizing the tensile mechanical properties (*i.e.*, Young's modulus, yield strength, strain-at-failure, and toughness) of dried PPU and PPU/CNC films.



This reduction was more evident in A21–40/CNC10, which is a likely result of more pronounced PBLA–CNC interactions with increasing PBLA content, restricting the chain mobility during deformation.

To facilitate understanding of the mechanism of mechanical reinforcement in PPU/CNC nanocomposites, their Young's moduli were compared with theoretical moduli predicted from both percolation and Halpin–Tsai (HT) models.<sup>68,69</sup> At 10 wt% of CNCs (above the percolation threshold =  $0.7/A^*$ , where  $A^*$  is the CNC aspect ratio  $\sim 10$ ), the experimental values of the nanocomposite films lie on or slightly below the modulus given by the HT model (Fig. S4†). This finding suggests that CNCs are randomly and homogeneously dispersed in the PPU matrices, and matrix–filler interactions are predominant over filler–filler interactions.<sup>69–71</sup> These favorable interfacial interactions between PPUs and CNCs may lead to an increase in the actual critical percolation threshold, preventing the formation of a 3D CNC network at 10 wt% of CNCs in PPUs.<sup>7</sup> Thus, prevalent PBLA–CNC hydrogen bonding significantly influenced not only self-assembly, but also mechanical behavior in PPU/CNC nanocomposites, suggesting that peptide–CNC interactions can be leveraged to tailor the mechanical properties in the dry state. Thus, it is anticipated that the hierarchical structures also will be correlated to the mechanical response to water.

### 3.5. Exploring the water-responsive behavior in mechanically tunable PPU-based materials: water uptake performance and mechanically adaptiveness

Water-responsive materials require absorption of water to alter their shape or properties. Hence, before exploring the mechanical response to water, we examined the aqueous swelling behavior of the dried films. The PEG chains are generally water-soluble and form loose coils in water as a result of hydrogen bonding between the ether oxygen atoms of PEG and hydrogen atoms of water molecules.<sup>72</sup> We observed that the PEG-based polyurea control without the PBLA blocks dissolved in water, preventing measurement of the degree of swelling. This behavior was expected due to the absence of a well-defined hard domain (*i.e.*, physically crosslinked network). Upon incorporation of the relatively hydrophobic PBLA segments, the films began to swell in water, indicating that the PBLA domains act as a physically-crosslinked net-point.<sup>73</sup> As shown in Table S1,† the uptake of water decreased from 780% to 195% with increasing PBLA content from 20 wt% to 40 wt%, which signifies decreased hydrophilicity. PBLA contains benzyl ester groups on the side chain, which can reduce water accessibility to the PBLA domains and stabilize physical crosslinking junctions in water. Remarkably, these non-chain extended PPUs exhibited a fast water absorption speed (within a minute) and a high swelling ratio compared to conventional thermoplastic polyether-based polyurethanes, which typically require  $\sim 5$  minutes to reach equilibrium water uptake (0.6%).<sup>4</sup> Upon

CNC addition into the PPU matrices, the maximum swelling ratio increased to 1080% for A21–20/CNC10 and 380% for A21–20/CNC20 (Table S1†), which can be ascribed to the presence of abundant hydroxyl groups on the CNC surface.<sup>11</sup> These results highlight that the addition of PBLA and/or CNC to conventional polymers enables tuning of water transport performance.

The water-responsive mechanical behavior of PPU and PPU/CNC films was investigated *via* DMA. Fig. 6A depicts the storage modulus ( $E'$ ) of PPUs and PPU/CNC nanocomposites as a function of time at room temperature. Upon immersion in water, all the PPU and PPU/CNC samples underwent a drastic reduction in the storage modulus. In peptide-containing materials and polymer/cellulose nanocomposites, the driving force for stiffness decrease upon exposure to water is generally the disruption of hydrogen bonding by water molecules.<sup>7,11,68</sup> Water molecules disrupt primarily filler–filler and matrix–filler interactions and weakly-bound hydrogen bonding (amorphous regions) in a polymer (matrix), but they tend not to diffuse into the physically-crosslinked net-point (*e.g.*, hard domains,  $\beta$ -sheet crystals).<sup>7,9,11,22,74,75</sup>

While the  $E'$  in the dry state ( $E'_{\text{dry}}$ ) of A21–20 was higher than that of A21–40 due to the higher PEG crystallinity in A21–20, the  $E'$  in the wet state ( $E'_{\text{wet}}$ ) of A21–20 was lower than that of A21–40. Increasing the PBLA content (A21–40) decreases hydrophilicity and allows for the formation of additional net-points or pseudo hard domains *via* peptidic ordering, leading to less disruption of the hydrogen-bonded domains by water molecules and resulting in only a slight reduction in the  $E'_{\text{wet}}$ .<sup>22</sup> It is noteworthy that PEG crystallinity is not linearly related to the wet-state storage modulus in PPUs. A21–20, which has a higher PEG crystallinity, exhibited a lower stiffness most likely due to the dominant influence of peptidic ordering on the mechanical behavior in the wet state. This observation suggests that PEG chains act as switching-points, whereas the PBLA blocks serve as the net-points in our material platform.

In contrast, the  $E'_{\text{dry}}$  of all nanocomposites were higher than that of the corresponding PPU matrices as a result of CNC reinforcement, whereas the  $E'_{\text{wet}}$  values of all nanocomposites were lower compared to the neat PPUs. These lower moduli of the nanocomposites are likely associated with variations in their hydrogen bonding arrangement. Based on ATR-FTIR and DSC data, CNC incorporation results in the disruption of peptidic ordering and a slight decrease in PEG crystallinity through PPU–CNC hydrogen bonding. These hydrogen bonding arrangements may be easily disrupted by water molecules, promoting more softening. Additionally, the morphology of the nanocomposites constructed *via* self-assembly of the matrix along CNC nanorods may facilitate the diffusion of water molecules. Thus, our water-responsive mechanical results highlight that modulating hierarchical organization *via* leveraging non-covalent interactions can be a design strategy to tailor mechanical response.



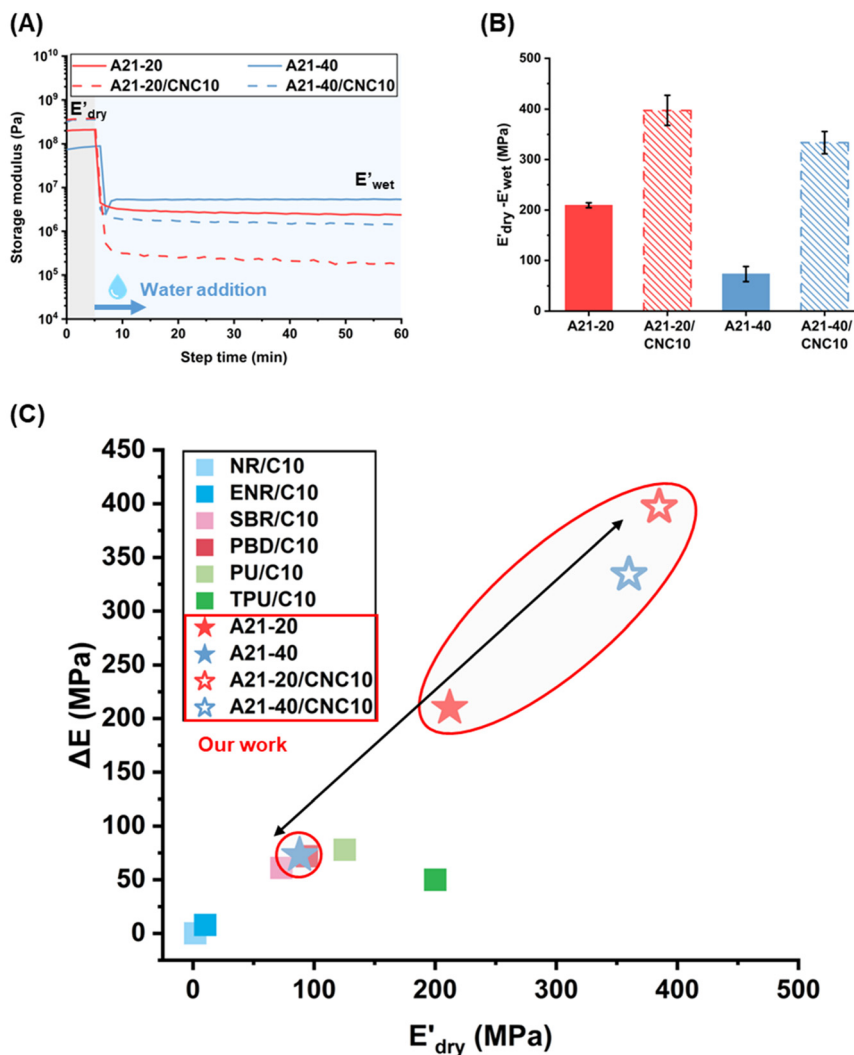


Fig. 6 (A) Storage modulus changes of the PPU and PPU/CNC films as a function of time. The samples were immersed in water ~5 minutes after testing started. (B) Bar graphs summarizing the water sensitivity,  $\Delta E(E'_{dry} - E'_{wet})$ . (C) Comparison of storage modulus in the dry state ( $E'_{dry}$ ) and water sensitivity ( $\Delta E$ ) of our materials (the PPUs and PPU/CNC nanocomposites: star shapes) with other reported polymer nanocomposites consisting of 10 wt% NC.<sup>4,7,10,68</sup> Our material platform exhibits a wide range of mechanical properties and water sensitivity.

To further evaluate the water-responsive mechanical adaptability quantitatively, the difference between  $E'_{dry}$  and  $E'_{wet}$  ( $\Delta E = E'_{dry} - E'_{wet}$ ) was used, which is a measure of the water-responsive sensitivity.<sup>7</sup> Fig. 6B shows that an increased PBLA content diminishes  $\Delta E$ , suggesting that peptide motifs control the sensitivity. On the contrary, the addition of CNCs led to a significant increase in the  $\Delta E$ , indicating the higher sensitivity of the nanocomposite compared to the matrix material due to the increased dynamic hydrogen bonding sites. Interestingly, the  $\Delta E$  differential between the neat PPUs and PPU/CNC nanocomposites was more drastic at higher PBLA content. The  $\Delta E$  of A21-40/CNC10 was 4.5× higher than that of A21-40, whereas the  $\Delta E$  of A21-20/CNC10 was ~2× higher than that of A21-20. This difference can be ascribed to a change in the extent of matrix-filler interactions. Increasing the PBLA content allows for more hydrogen bonding sites associated with CNCs. The presence of more

PBLA-CNC interactions can lead to a more significant change in the  $\Delta E$ , revealing that the matrix-filler interactions can be controlled through varying the peptide content in the peptidic hybrid/cellulose nanocomposites. Thus, this finding implies that peptide-cellulose interactions can be used as a handle to tailor the sensitivity to water. Furthermore, the tunable sensitivity of our material platform extends beyond the property space of water-responsive, mechanically-adaptive polymer/cellulose nanocomposites reported previously (Fig. 6C and Table S2†). Our matrix materials (PPUs) exhibit water-triggered softening behavior, unlike conventional polymer matrices ( $\Delta E = \sim$  zero), emphasizing the potential of peptide motifs in the design of tunable water-responsive materials. Overall, this water-responsive behavior highlights that our engineering strategy allows for the development of adaptable materials with tunable stiffness changes, ranging from ~70 MPa to ~400 MPa.





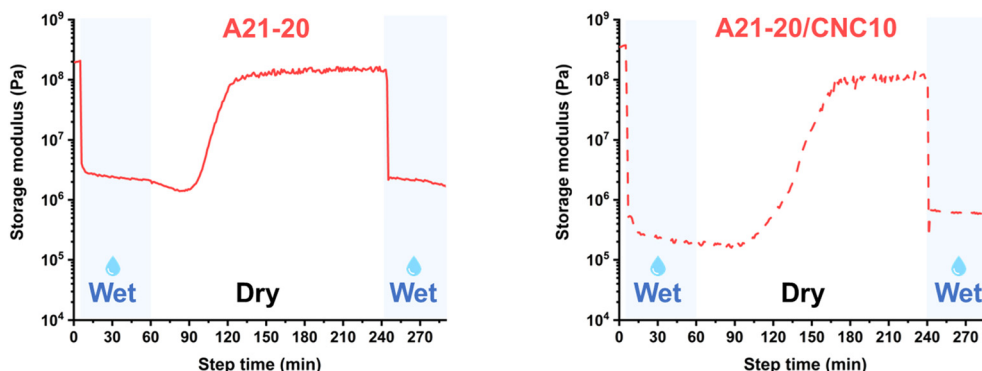


Fig. 7 Representative PPUs (A21-20) and PPU/CNC nanocomposites (A21-20/CNC10) showing the reversible variation of the storage modulus during drying–wetting–drying–wetting cycles. Throughout the drying cycle, the films were left to air-dry in ambient air at room temperature for 180 min.

The reversibility of mechanical response using A21-20 and A21-20/CNC10 also was probed. Upon removal of water (Fig. 7), the  $E'$  increases gradually and recovered almost to the original  $E'$  value, indicating the re-formation of disassociated hydrogen bonds. A subsequent wetting step indicates the reversible disruption of this hierarchical, hydrogen-bonded morphology. Thus,  $E'$  can be reversibly switched between the wet (water exposure) and dry states (water removal) in these PPU/CNC nanocomposites.

## 4. Conclusion

In this research, we have successfully demonstrated the molecular design of silk-inspired nanocomposites for engineering water-responsive and mechanically switching materials. This new class of nanocomposites, comprised of a peptide-containing polymer matrix and nanocellulose, exhibited diverse hierarchical ordering and tailorable water-responsive behavior through modulation of the extent of matrix–filler interactions. Unlike conventional matrix materials in water-responsive nanocomposites, our matrix materials (*i.e.*, PPUs) displayed tunable modulus switching in response to water. The water sensitivity ( $\Delta E$ ) of PPUs was dictated by the peptidic ordering, which served as physically-crosslinked junctions. Higher PBLA content increased the density of the peptide phase, thereby diminishing the water sensitivity. Incorporating CNCs into the PPUs varied the hydrogen bonding arrangements and morphologies of PPUs primarily *via* peptide–cellulose interactions, amplifying their mechanical stiffening and softening effects in the dry and wet states, respectively. These new non-covalent interactions yielded interlocking morphologies, increasing water sensitivity compared to the PPU matrices. Our material platform enabled the development of adaptive materials with an extended range of water-responsive storage modulus differential, ranging from approximately 70 MPa to 400 MPa. This research highlights that precise control of peptidic ordering and peptide–cellulose interactions enables tuning of not only mechanical performance, but also water sensitivity. This design approach can be applied to other synthetic,

passive polymers to create dynamic materials for diverse applications, including smart textiles, membranes, soft robots, and scaffolds.

## Data availability

The data supporting this article have been included as part of the ESI.†

## Conflicts of interest

The authors declare no conflict of interest.

## Acknowledgements

Financial support for this research was provided by the National Science Foundation (NSF) PIRE: Bio-inspired Materials and Systems [OISE 1844463]. DMA studies were supported as part of the Center for Plastics Innovation, an Energy Frontier Research Center funded by the U.S. Department of Energy, Office of Science, Basic Energy Sciences, under award DE-SC0021166, for the use of RSA-G2 instrument. AFM access was supported by the Delaware INBRE program, with grants from the NIH-NIGMS (#P20 GM103446) and the State of Delaware, and it was provided by the BioImaging Center at the University of Delaware. Access to the ATR-FTIR, DSC, and SAXS was provided by the Advanced Materials Characterization Laboratory (AMCL) at the University of Delaware. We thank <https://www.BioRender.com> for providing tools that facilitated the creation of several figures included in this manuscript.

## References

- 1 P. K. Annamalai, K. L. Dagnon, S. Monemian, E. J. Foster, S. J. Rowan and C. Weder, *ACS Appl. Mater. Interfaces*, 2014, **6**, 967–976.
- 2 Y. Cui, L. Li, C. Liu, Y. Wang, M. Sun, B. Jia, Z. Shen, X. Sheng and Y. Deng, *Nano Lett.*, 2023, **23**, 11693–11701.
- 3 J. Yi, G. Zou, J. Huang, X. Ren, Q. Tian, Q. Yu, P. Wang, Y. Yuan, W. Tang, C. Wang, L. Liang, Z. Cao, Y. Li, M. Yu, Y.



- Jiang, F. Zhang, X. Yang, W. Li, X. Wang, Y. Luo, X. J. Loh, G. Li, B. Hu, Z. Liu, H. Gao and X. Chen, *Nature*, 2023, **624**, 295–302.
- 4 Y. Wang, Z. Cheng, Z. Liu, H. Kang and Y. Liu, *J. Mater. Chem. B*, 2018, **6**, 1668–1677.
  - 5 P. Awasthi and S. S. Banerjee, *Polymer*, 2022, **259**, 125338.
  - 6 L. Hsu and S. J. Rowan, *J. Mater. Chem.*, 2011, **41**, 2812–2822.
  - 7 M. Tian, X. Zhen, Z. Wang, H. Zou, L. Zhang and N. Ning, *ACS Appl. Mater. Interfaces*, 2017, **9**, 6482–6487.
  - 8 J. R. Capadona, K. Shanmuganathan, D. J. Tyler, S. J. Rowan and C. Weder, *Science*, 2008, **319**, 1370–1374.
  - 9 K. Shanmuganathan, J. R. Capadona, S. J. Rowan and C. Weder, *Prog. Polym. Sci.*, 2010, **35**, 212–222.
  - 10 K. L. Dagnon, K. Shanmuganathan, C. Weder and S. J. Rowan, *Macromolecules*, 2012, **45**, 4707–4715.
  - 11 J. Mendez, P. K. Annamalai, S. J. Eichhorn, R. Rusli, S. J. Rowan, E. J. Foster and C. Weder, *Macromolecules*, 2011, **44**, 6827–6835.
  - 12 C. B. Thompson and L. T. J. Korley, *ACS Macro Lett.*, 2020, **9**, 1198–1216.
  - 13 H. Huang, J. Hu and Y. Zhu, *Macromol. Biosci.*, 2013, **13**, 161–166.
  - 14 L. Gu, Y. Jiang and J. Hu, *Mater. Today: Proc.*, 2019, **16**, 1491–1496.
  - 15 L. Gu, Y. Jiang and J. Hu, *Appl. Sci.*, 2017, **7**, 1258–1265.
  - 16 P. K. Gavel, D. Dev, H. S. Parmar, S. Bhasin and A. K. Das, *ACS Appl. Mater. Interfaces*, 2018, **10**, 10729–10740.
  - 17 D. Jang, C. B. Thompson, S. Chatterjee and L. T. J. Korley, *Mol. Syst. Des. Eng.*, 2021, **6**, 1003–1015.
  - 18 L. Gu, Y. Jiang, L. M. C. Chow, Z. Liu, W. Gao, Y. Han, C. Wang and J. Hu, *Mater. Des.*, 2022, **219**, 110761.
  - 19 L. Gu, Y. Jiang and J. Hu, *Polymer*, 2018, **10**, 637–648.
  - 20 Z. Wang, S. Kang, S. Cao, M. Krecker, V. V. Tsukruk and S. Singamaneni, *MRS Bull.*, 2020, **45**, 1017–1026.
  - 21 M. K. Gupta, D. T. Wagner and M. C. Jewett, *MRS Bull.*, 2020, **45**, 999–1004.
  - 22 L. Gu, Y. Jiang and J. Hu, *Mater. Today Commun.*, 2018, **17**, 419–426.
  - 23 Y. Feng, X. Li, M. Li, D. Ye, Q. Zhang, R. You and W. Xu, *ACS Sustainable Chem. Eng.*, 2017, **5**, 6227–6236.
  - 24 Y. M. Abul-Haija and R. V. Ulijn, *Biomacromolecules*, 2015, **16**, 3473–3479.
  - 25 R. Xiong, H. S. Kim, S. Zhang, S. Kim, V. F. Korolovych, R. Ma, Y. G. Yingling, C. Lu and V. V. Tsukruk, *ACS Nano*, 2017, **11**, 12008–12019.
  - 26 J. E. Semple, B. Sullivan and K. N. Sill, *Synth. Commun.*, 2017, **47**, 53–61.
  - 27 L. E. Matolyak, J. K. Keum, K. M. Van De Voorde and L. T. J. Korley, *Org. Biomol. Chem.*, 2017, **15**, 7607–7617.
  - 28 L. T. J. Korley, S. M. Liff, N. Kumar, G. H. McKinley and P. T. Hammond, *Macromolecules*, 2006, **39**, 7030–7036.
  - 29 C. Calvino, N. Macke, R. Kato and S. J. Rowan, *Prog. Polym. Sci.*, 2020, **103**, 101221.
  - 30 C. Czeslik and A. Wittemann, *Colloid Polym. Sci.*, 2020, **298**, 775–789.
  - 31 S. Tanaka, A. Ogura, T. Kaneko, Y. Murata and M. Akashi, *Macromolecules*, 2004, **37**, 1370–1377.
  - 32 S. A. Riou, S. L. Hsu and H. D. Stidham, *Biophys. J.*, 1998, **75**, 2451–2460.
  - 33 G. Floudas and P. Papadopoulos, *Macromolecules*, 2003, **36**, 3673–3683.
  - 34 J. C. Johnson, N. D. Wanasekara and L. T. J. Korley, *J. Mater. Chem. B*, 2014, **2**, 2554–2561.
  - 35 L. T. J. Korley, B. D. Pate, E. L. Thomas and P. T. Hammond, *Polymer*, 2006, **47**, 3073–3082.
  - 36 S.-W. Kuo and C.-J. Chen, *Macromolecules*, 2011, **44**, 7315–7326.
  - 37 Y. Kou, S. Wang, J. Luo, K. Sun, J. Zhang, Z. Tan and Q. Shi, *J. Chem. Thermodyn.*, 2019, **128**, 259–274.
  - 38 J. Tang, M. Yang, W. Dong, M. Yang, H. Zhang, S. Fan, J. Wang, L. Tan and G. Wang, *RSC Adv.*, 2016, **6**, 40106–40114.
  - 39 E. Yilgör, E. Burgaz, E. Yurtsever and I. Yilgör, *Polymer*, 2000, **41**, 849–857.
  - 40 L. E. Matolyak, C. B. Thompson, B. Li, J. K. Keum, J. E. Cowen, R. S. Tomazin and L. T. J. Korley, *Biomacromolecules*, 2018, **19**, 3445–3455.
  - 41 M. R. Kim, H. J. Park, K. H. Cheon, C. K. Yeom and K. Y. Lee, *Sci. Rep.*, 2020, **10**, 1–11.
  - 42 K. Ishino, H. Shingai, Y. Hikita, I. Yoshikawa, H. Houjou and K. Iwase, *ACS Omega*, 2021, **6**, 32869–32878.
  - 43 Z. Yang, H. Peng, W. Wang and T. Liu, *J. Appl. Polym. Sci.*, 2010, **116**, 2658–2667.
  - 44 A. Saralegi, L. Rueda, L. Martin, A. Arbelaiz, A. Eceiza and M. A. Corcuera, *Compos. Sci. Technol.*, 2013, **88**, 39–47.
  - 45 M. Nagalakshmaiah, F. Pignon, N. El Kissi and A. Dufresne, *RSC Adv.*, 2016, **6**, 66224–66232.
  - 46 S. S. Shazleen, T. A. T. Yasim-Anuar, N. A. Ibrahim, M. A. Hassan and H. Ariffin, *Polymer*, 2021, **13**, 1–19.
  - 47 M. Gu, C. Jiang, D. Liu, N. Prempeh and I. I. Smalyukh, *ACS Appl. Mater. Interfaces*, 2016, **8**, 32565–32573.
  - 48 C. C. Fu, C. Y. Wu, C. C. Chien, T. H. Hsu, S. F. Ou, S. T. Chen, C. H. Wu, C. Te Hsieh, R. S. Juang and Y. H. Hsueh, *Nanomaterials*, 2020, **10**, 1–15.
  - 49 H. Xiang, S. Wang, R. Wang, Z. Zhou, C. Peng and M. Zhu, *Sci. China:Chem.*, 2013, **56**, 716–723.
  - 50 T. Komoto, M. Oya and T. Kawai, *Makromol. Chem.*, 1974, **175**, 301–310.
  - 51 Y. Wu, L. Li, S. Chen, J. Qin, X. Chen, D. Zhou and H. Wu, *Sci. Rep.*, 2020, **10**, 1–12.
  - 52 S. Pongkitwitoon, R. Hernández, J. Weksler, A. Padsalgikar, T. Choi and J. Runt, *Polymer*, 2009, **50**, 6305–6311.
  - 53 M. Song, H. S. Xia, K. J. Yao and D. J. Hourston, *Eur. Polym. J.*, 2005, **41**, 259–266.
  - 54 Q. Tian, I. Krakovský, G. Yan, L. Bai, J. Liu, G. Sun, L. Rosta, B. Chen and L. Almásy, *Polymer*, 2016, **8**, 197.
  - 55 M. Villani, R. Consonni, M. Canetti, F. Bertoglio, S. Iervese, G. Bruni, L. Visai, S. Iannace and F. Bertini, *Polymer*, 2020, **12**, 362.
  - 56 G. Floudas and H. W. Spiess, *Macromol. Rapid Commun.*, 2009, **30**, 278–298.



- 57 J. C. Johnson, N. D. Wanasekara and L. T. J. Korley, *Biomacromolecules*, 2012, **13**, 1279–1286.
- 58 A. Pournaghshband Isfahani, M. Shahrooz, T. Yamamoto, A. Muchtar, M. M. Ito, D. Yamaguchi, M. Takenaka, E. Sivaniah and B. Ghalei, *RSC Adv.*, 2021, **11**, 15449–15456.
- 59 P. S. De Oliveira Patricio, I. M. Pereira, N. C. F. Da Silva, E. Ayres, F. V. Pereira and R. L. Oréface, *Eur. Polym. J.*, 2013, **49**, 3761–3769.
- 60 P. Khadivi, M. S. Kalajahi, H. R. Mamaqani, R. Lotfi and M. Sofla, *Appl. Phys. A: Mater. Sci. Process.*, 2019, **125**, 1–10.
- 61 H. Cao, F. Qi, R. Liu, F. Wang, C. Zhang, X. Zhang, Y. Chai and L. Zhai, *RSC Adv.*, 2017, **7**, 11244–11252.
- 62 J. Chen, C. Li, H. Jia, Z. Shen, R. Zhao, T. Su, B. Xiang, X. Wang, D. W. Boukhvalov, Z. Luo and Y. Luo, *Macromolecules*, 2022, **55**, 4776–4789.
- 63 S. Qin, Y. Hu, X. Tian, Y. Tian, W. Liu and L. Zhao, *Cellulose*, 2020, **27**, 4337–4353.
- 64 B. X. Cheng, W. C. Gao, X. M. Ren, X. Y. Ouyang, Y. Zhao, H. Zhao, W. Wu, C. X. Huang, Y. Liu, X. Y. Liu, H. N. Li and R. K. Y. Li, *Polym. Test.*, 2022, **107**, 107489.
- 65 C. M. Koo, M. A. Hillmyer and F. S. Bates, *Macromolecules*, 2006, **39**, 667–677.
- 66 R. S. Waletzko, L. T. J. Korley, B. D. Pate, E. L. Thomas and P. T. Hammond, *Macromolecules*, 2009, **42**, 2041–2053.
- 67 F. Wu, L. Chen, Y. Li, K. I. Lee and B. Fei, *J. Mater. Sci.*, 2017, **52**, 4421–4434.
- 68 Y. Zhu, J. Hu, H. Luo, R. J. Young, L. Deng, S. Zhang, Y. Fan and G. Ye, *Soft Matter*, 2012, **8**, 2509–2517.
- 69 A. Redondo, N. Mortensen, K. Djeghdi, D. Jang, R. D. Ortuso, C. Weder, L. T. J. Korley, U. Steiner and I. Gunkel, *ACS Appl. Mater. Interfaces*, 2022, **14**, 7270–7282.
- 70 A. Peterson, A. Y. Mehandzhiyski, L. Svenningsson, A. Ziolkowska, K. Roland, A. Lund, L. Sandblad, L. Even, G. Lo Re, I. Zozoulenko and C. Mu, *Macromolecules*, 2021, **54**, 3507–3516.
- 71 K. Shanmuganathan, J. R. Capadona, S. J. Rowan and C. Weder, *ACS Appl. Mater. Interfaces*, 2010, **2**, 165–174.
- 72 M. L. Alessi, A. I. Norman, S. E. Knowlton, D. L. Ho and S. C. Greer, *Macromolecules*, 2005, **38**, 9333–9340.
- 73 Y. Park, Y. W. Choi, S. Park, C. S. Cho, M. J. Fasolka and D. Sohn, *J. Colloid Interface Sci.*, 2005, **283**, 322–328.
- 74 M. Jorfi, M. N. Roberts, E. J. Foster and C. Weder, *ACS Appl. Mater. Interfaces*, 2013, **5**, 1517–1526.
- 75 S. S. Banerjee, S. Hait, T. S. Natarajan, S. Wießner, K. W. Stöckelhuber, D. Jehnichen, A. Janke, D. Fischer, G. Heinrich, J. J. C. Busfield and A. Das, *J. Phys. Chem. B*, 2019, **123**, 5168–5175.

